buildings

MDPI

Article

Experimental Investigation on the Effect of Wetting–Drying Cycles on Bond Performance of GFRP Adhesive Anchors in Concrete

Yifan Xu [1], Wensheng Liang [2,3,*], Xianghong Ding [1] and Yanjie Wang [4]

[1] College of Civil Engineering & Architecture, China Three Gorges University, Yichang 443000, China; xuyifan@ctgu.edu.cn (Y.X.)
[2] School of Architectural and Hydraulic Engineering, Jiujiang Polytechnic University of Science and Technology, Jiujiang 332020, China
[3] Institute of Management and Business Named After A.A. Asanova, Kyrgyz National University Named After Jusup Balasagyn, Bishkek 720033, Kyrgyzstan
[4] Department of Mechanical Engineering, The University of Western Australia, Perth, WA 6009, Australia
* Correspondence: wsl2025228@163.com

Abstract

The long-term durability of adhesive anchors in aggressive environments is a critical concern for infrastructure safety, with steel corrosion being one of the most detrimental phenomena. While glass fiber-reinforced polymer (GFRP) anchors offer corrosion-resistant alternatives to steel anchors in harsh marine environments, the bond performance at the anchorage interface progressively deteriorates under wetting–drying (WD) cycles, which may compromise long-term anchorage integrity. However, the bond characteristics of GFRP anchors under WD exposure, particularly the development of predictive models, remain insufficiently understood. This paper presents an experimental investigation into the impact of WD cycles on the bond of GFRP adhesive anchors in concrete. Twenty-four specimens were tested under pull-out loads, considering two key variables: bonded length (40 mm and 80 mm, corresponding to 5 and 10 times the bar diameter) and number of WD cycles (0, 30, 60, and 90). Artificial seawater was prepared via ASTM D1141-98 to simulate marine exposure conditions. The results revealed that both bond strength and bond stiffness decreased significantly with increasing WD cycles, while the failure mode progressively shifted from the bar–adhesive interface to the adhesive–concrete interface. Based on the experimental data, a cycle-dependent bond strength model was developed to predict the bond degradation of the anchor–concrete interface after WD exposure. Requiring only the undegraded concrete strength, the proposed model effectively captures the coupled effects of WD cycles and bonded length on bond strength degradation, presenting a practical tool for the durability design and service life evaluation of GFRP anchorage systems in coastal and marine environments.

Keywords: GFRP adhesive anchor; wetting–drying cycles; bond degradation; failure mode; bond strength model

Check for updates

Academic Editor: Antonio Caggiano

Received: 13 March 2026
Revised: 14 April 2026
Accepted: 16 April 2026
Published: 22 April 2026

Copyright: © 2026 by the authors. Licensee MDPI, Basel, Switzerland. This article is an open access article distributed under the terms and conditions of the Creative Commons Attribution (CC BY) license.

1. Introduction

Glass fiber-reinforced polymer (GFRP) anchors have been recognized as a promising alternative to steel anchors in concrete structures exposed to aggressive environments [1–3]. In anchorage applications, GFRP adhesive anchors are extensively employed for structural

retrofitting, strengthening, and the connection of non-structural elements in existing concrete structures [4,5]. Compared to the traditional retrofitted techniques, GFRP adhesive anchorages are more attractive because of larger concrete covers and greater contact regions with the surrounding substrate [6]. This geometric configuration is shown to provide superior protection to the bonded area exposed to aggressive environmental exposure, as the thicker concrete cover can delay the ingress of moisture and aggressive ions, while the larger contact area may enhance load transfer efficiency [7]. Consequently, GFRP adhesive anchor systems are anticipated to offer enhanced durability in marine environments compared to other FRP bonding techniques.

The load transfer mechanism in a GFRP adhesive anchor system is inherently complex, governed by the mechanical interaction across two distinct interfaces: the concrete-to-adhesive interface and the adhesive-to-GFRP bar interface. Nevertheless, the long-term performance of GFRP adhesive anchors in marine environments remains a critical concern for infrastructure safety. Coastal and offshore structures are routinely subjected to WD cycles in tidal and splash zones, where alternating immersion in seawater and exposure to air creates one of the most aggressive exposure conditions for concrete structures [8,9]. Under such cyclic exposure, the bond performance at the interfaces progressively deteriorates through multiple coupled degradation mechanisms. First, the epoxy adhesive layer undergoes hydrolysis and plasticization due to moisture ingress, leading to reduced mechanical properties and weakened adhesion to both the GFRP bar and the concrete substrate [10,11]. Second, the concrete interfacial transition zone (ITZ) is attacked by chloride and sulfate ions, causing softening of calcium–silicate–hydrate (C-S-H) gels, leaching of calcium hydroxide, and the formation of expansive products that generate microcracks [12,13]. Third, the resin matrix of the GFRP bar surface experiences hydrolysis and osmotic cracking, compromising the integrity of the sand-coated layer and reducing its mechanical interlock capacity [14,15].

The FRP adhesive anchor system, where an FRP bar is adhesively bonded into a pre-drilled hole through the concrete section, is also known as the embedded through-section (ETS) strengthening technique. Hereafter, this system is referred to as the ETS FRP system for brevity. Three main FRP strengthening techniques exist for concrete structures: externally bonded (EB) using FRP sheets or plates, near-surface-mounted (NSM) using FRP bars placed in grooves, and the ETS technique used in this study, where an FRP bar is adhesively bonded into a drilled hole [14,15]. Among these, the ETS method investigated in the present study provides a much larger concrete cover and greater contact area with the surrounding substrate than EB or NSM systems, which is expected to enhance durability under aggressive environmental exposure. While the short-term bond behavior of ETS FRP reinforcements has been extensively studied [12–15], research into their durability under WD cycles is focused on carbon FRP (CFRP) or basalt FRP (BFRP) composites based on EB and NSM methods [16]. For instance, Garzón-Roca et al. [17] observed a significant degradation in the interfacial bond behavior of NSM FRP bars within the first 30 WD cycles, after which the degradation rate stabilized. Wang et al. [18] reported that WD cycling in seawater resulted in substantial degradations on the interface between EB CFRP sheets and high-strength concrete, with the bond parameters progressively diminishing as the number of cycles increases. Noor-E-Khuda [19] investigated the effect of WD cycles on the compressive, flexural, and pull-out bond strengths of mortar and developed the correlation between material strengths and bond strengths. Cui et al. [20], Wei et al. [21], and Al-Lami et al. [22] studied the bond performance of EB CFRP–concrete and BFRP–concrete interfaces exposed to WD cycles and proposed time-dependent bond stress–slip models used for practical design. Xie et al. [23,24] experimentally evaluated the effect of WD cycles on the fatigue bond behavior of BFRP–concrete interfaces.

Reliable bond strength models are essential not only for predicting the remaining load-carrying capacity of existing anchors after years of environmental exposure, but also for enabling accurate numerical simulations of anchor behavior under service loads. Furthermore, such models serve as indispensable tools for performance-based durability design, allowing engineers to select appropriate anchor dimensions and configurations to achieve desired service lives under given environmental conditions [24]. As highlighted by Cunha Jr. et al. [25], deterministic failure criteria may not always be the most conservative when parameter variability is taken into account. This perspective underscores the need for empirical models that are not only calibrated against experimental data but also accompanied by clear statements of their applicability limits, especially when predicting long-term performance under uncertain environmental conditions.

To date, all existing studies on the bond durability of FRP–adhesive–concrete interfaces under WD cycles have focused exclusively on EB or NSM configurations [17–24]. No study has investigated the ETS system under such exposure. While some studies have examined the bond durability of two-phase systems (FRP bar directly bonded to concrete without an adhesive layer) [8,26] under WD cycles, those findings cannot be directly applied to the ETS method for two reasons. First, the presence of an epoxy adhesive layer transforms the original single interface (FRP bar directly bonded to concrete) into two distinct interfaces: the FRP bar–adhesive interface and adhesive–concrete interface. This fundamentally alters the bond failure mechanism, as debonding may initiate and propagate along either interface depending on their relative degradation. Second, the epoxy adhesive is susceptible to degradation under WD cycles. As reported by Wang et al. [18], the tensile strength and elastic modulus of epoxy adhesive decreased substantially with increasing WD cycles, and brittle fracture became more pronounced due to hydrolysis and plasticization. Such degradation directly weakens both interfaces and compromises the overall load transfer capacity. Therefore, the bond degradation mechanisms in the ETS system remain unknown, and no bond strength degradation model currently exists for this configuration under WD cycles. Conclusively, a clear research gap exists in that the bond durability of the GFRP bar–adhesive–concrete system under WD cycles has not been experimentally quantified, and no design-oriented bond strength degradation model is available for this system.

To address this critical research gap, this study conducted an experimental investigation into the bond behavior of adhesively bonded GFRP anchors in concrete subjected to simulated marine WD cycles. Standard pull-out specimens were fabricated and tested under pull-out loading. Two tested variables including the number of WD cycles and the bonded length were considered. The main novelty and contribution of this study is fourfold. First, the bond degradation between adhesively bonded FRP bars and concrete under simulated marine WD cycles is experimentally quantified for a configuration not previously studied. Second, the progressive shift in failure modes from the bar–adhesive interface to adhesive–concrete interface as WD cycles increase is identified. Third, a quantitative comparison with NSM systems reported in the literature [27] is provided, highlighting the better protective effect in the ETS system. Fourth, a bond strength degradation model that explicitly accounts for the number of WD cycles and bonded length for ETS systems is developed and validated for the first time. Unlike existing models that focus on EB/NSM configurations or two-phase systems without an adhesive layer, the proposed model is tailored for ETS systems and requires only the undegraded compressive strength of concrete as input, offering a practical tool for the durability design of ETS-strengthened structures in coastal and marine environments.

2. Experimental Program

A total of 24 pull-out specimens were prepared, comprising 8 test groups with three replicates per group. The tested variables included the number of WD cycles (0, 30, 60, and 90) and the bonded length (40 mm and 80 mm, corresponding to 5 and 10 times the bar diameter, respectively).

2.1. Materials

2.1.1. GFRP Bar

Sand-coated GFRP bars of 8 mm diameter were employed, manufactured by Haichuan New Materials Co., Ltd., Shenzhen, China. The bars were composed of continuous glass fibers and phenolic resin matrix, with nylon winding and sand coating on the surface. The geometric and mechanical properties of the bars, as provided by the manufacturer, are summarized in Table 1. For tensile testing, both ends of each bar were embedded in epoxy-filled steel tubes (length: 300 mm, outer diameter: 35 mm, and wall thickness: 5 mm), resulting in a free gauge length of 400 mm. All tests were performed in accordance with ASTM D3916-08 [28]. As illustrated in Figure 1, the specimens were loaded at displacement rates of 2 mm/min via a WAW-2000D universal testing machine (manufactured by Jinan Zhonglu Chang testing machine Manufacturing Co., Ltd., Jinan, China). Axial deformation was continuously recorded using an extensometer with a 100 mm gauge length attached directly to the rebar. The elastic modulus was tested by utilizing a linear regression to the stress–strain curves over strain ranges of 0.001 to 0.003 [28]. A total of five replicate specimens were tested for each group.

Table 1. Tensile properties of GFRP bar (average ± standard deviation).

Bar Diameter (mm)	Tensile Strength f_y (MPa)	Elastic Modulus E_t (GPa)	Rib Height (mm)	Rib Spacing (mm)
8.78	1198 ± 32.6	51.4 ± 2.92	0.10	9.17

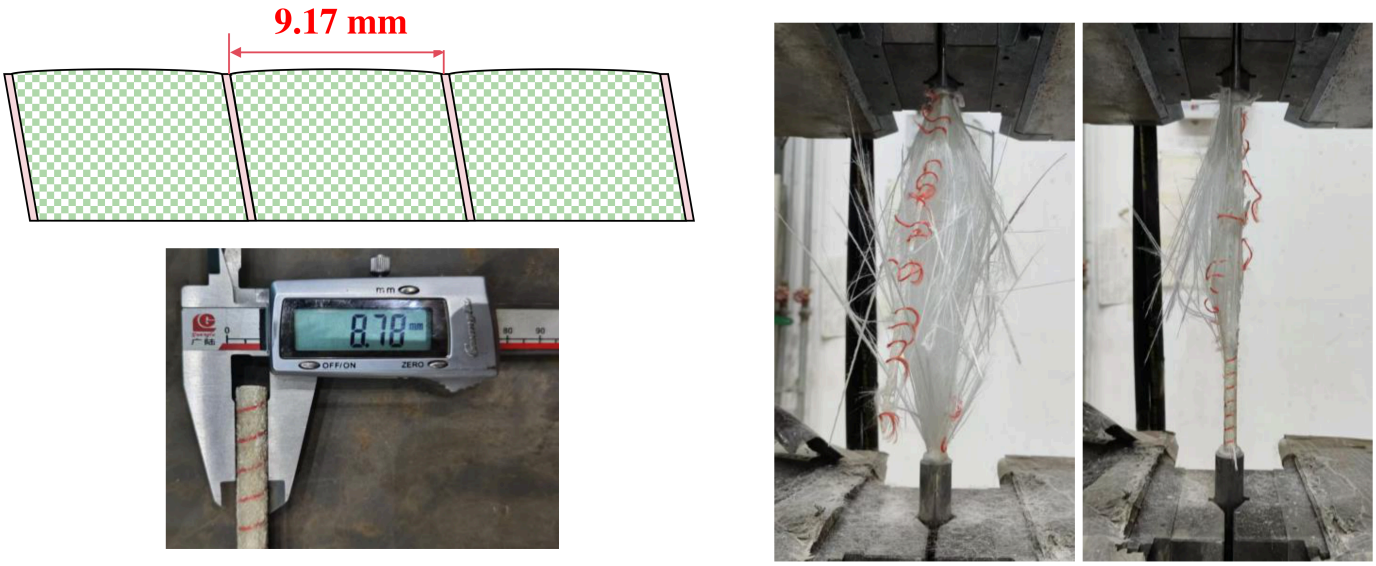

(a) Rib geometry and dimensions (b) Tensile testing

Figure 1. (**a**) Dimension details; and (**b**) tensile testing of GFRP bar (dimensions in mm).

2.1.2. Concrete

Concrete with a nominal compressive strength grade of C50 was designed according to JGJ 55-2011 [29]. The mix proportions are presented in Table 2. Ordinary Portland cement (P.O. 42.5) produced by Wuan Ruiyun Cement Co., Ltd., Handan, China, was used. Natural marble chips with a particle size of 5–10 mm were employed as coarse aggregate, and river sand with a maximum diameter of 1.25 mm was used as fine aggregate. The 100 mm cubes were prepared and tested according to GB/T 50081-2019 [30] to determine the 28-day compressive and splitting tensile strengths, as shown in Figure 2. The elastic modulus was measured by using prism-shaped samples with dimensions of 300 × 100 × 100 mm^3. All material property values were measured after 28 days of curing. The average results are summarized in Table 3. The 28-day compressive strength ($f_{c,0}$ = 53.96 MPa) was employed as the undegraded reference value for subsequent bond strength normalization in Section 4.

Table 2. Mix proportion of concrete.

Strength Grade	Cement (kg/m^3)	Sand (kg/m^3)	Water (kg/m^3)	Coarse Aggregate (kg/m^3)
C50	433	603	195	1170



(a) (b)

Figure 2. (**a**) Tested specimens; and (**b**) compressive and splitting tensile tests of concrete.

Table 3. Mechanical parameters of C50 concrete (average ± standard deviation).

Strength Grade	Compressive Strength (MPa)	Tensile Splitting Strength (MPa)	Elastic Modulus (GPa)
C50	53.96 ± 4.65	3.73 ± 0.26	34.53 ± 0.21

2.1.3. Adhesive

A two-component epoxy-based injection adhesive (MPZZ-A/B) manufactured by Yalai Shi New Materials Co., Ltd., Tianjin, China, was employed for bonding the GFRP

anchors to concrete. The mix ratio of Component A to Component B was 2:1 by weight. The mechanical parameters of the cured epoxy adhesive were experimentally determined according to the Chinese standard GB/T 2567-2008 [31], as shown in Figure 3. Resin-cast specimens were prepared and tested under tensile loading to obtain the results of tensile strength, elastic modulus, and elongation. Six replicate specimens were tested. The results are summarized in Table 4. The compressive strength, flexural strength, and steel-to-steel shear strength of the adhesive were provided by the manufacturer as 98.5, 77.6, and 21.9 MPa, respectively.

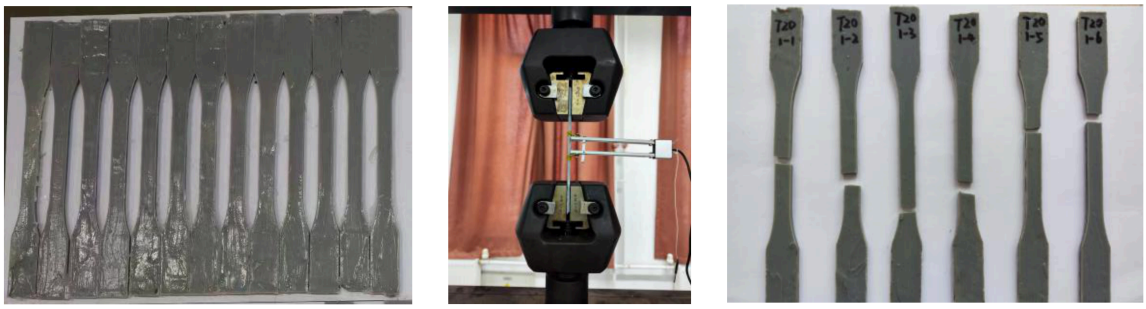

(a) Tensile specimens (b) Tensile tests (c) Failure mode

Figure 3. (**a**) Tested specimens; (**b**) tensile tests; and (**c**) failure mode of epoxy adhesive.

Table 4. Tensile parameters of adhesive (average ± standard deviation).

Tensile Strength (MPa)	Elastic Modulus (GPa)	Elongation at Break (%)
18.65 ± 1.57	5.94 ± 0.30	3.14 ± 0.22

2.1.4. Artificial Seawater

Artificial seawater was prepared following ASTM D1141-98 [32] to simulate the marine environment. The chemical composition is detailed in Table 5. The solution was prepared by first mixing a base solution containing NaCl and Na_2SO_4, followed by the addition of Solution 1 (containing $MgCl_2$ and $CaCl_2$) and Solution 2 (containing KCl and $NaHCO_3$). The mixture was then diluted with tap water to the required volume. For a total volume of 141.6 L, the solution was prepared as follows.

Table 5. Chemical composition of artificial seawater (g/L) [33].

NaCl	$MgCl_2$	Na_2SO_4	$CaCl_2$	KCl	$NaHCO_3$
24.53	5.20	4.09	1.16	0.70	0.20

(i) Base solution: 3474.01 g of NaCl and 579.71 g of Na_2SO_4 were dissolved in 120.36 L of tap water.
(ii) Solution 1: 736.78 g of $MgCl_2$ and 163.97 g of $CaCl_2$ were dissolved in 2.83 L of tap water and then added to the base solution.
(iii) Solution 2: 98.41 g of KCl and 28.46 g of $NaHCO_3$ were dissolved in 1.42 L of tap water and then added to the mixture.
(iv) Dilution: The combined solution was diluted with an additional 17 L of tap water to reach the final volume of 141.6 L. The chemical composition of the artificial seawater is summarized in Table 5. This mixture has been applied and validated in the literature [33].

2.2. Specimen Fabrication

To quantify the bond behavior under marine WD cycles, concentric pull-out specimens were designed. In the preparation of pull-out specimens, vertical holes were created along the centerlines of the concrete samples via PVC tubes before concrete casting. To achieve the desired bonded length, the PVC tubes were positioned to define the unbonded zones at both ends. Prior to inserting the GFRP bars, a thin layer of sponge was placed between the PVC tube and the bar as a barrier to prevent adhesive from entering the unbonded parts. When ready for bonding, the PVC tube segment near the loaded end was removed to allow adhesive injection from the embedded end using a narrow nozzle. During injection, each GFRP bar was slowly twisted and pushed vertically into the hole to eliminate trapped air pockets. The injection process was stopped as soon as the adhesive reached the unbonded region near the loaded end. That region was then sealed with a PVC tube filled with sponge to contain the adhesive within the intended bonded length. More detailed procedures can be found in Liu et al. [12].

The specimen geometry and dimensions followed the Chinese standard GB/T 30022-2013 [34]. The concrete substrates were cast as 100 mm × 100 mm × 150 mm prisms. GFRP bars with a total length of 500 mm were embedded concentrically. As shown in Figure 4, two different bonded lengths were achieved by using polyvinyl chloride (PVC) tubes and Teflon tape to create unbonded zones at both ends, preventing stress concentration at the loaded end. The bonded lengths were set to 40 mm (5 times the bar diameter) and 80 mm (10 times the bar diameter). To prevent crushing of the GFRP bar by the testing machine grips, the loaded end was protected using the seamless steel tube (length: 200 mm; outer diameter: 25 mm; and wall thickness: 3 mm) filled with epoxy resin. A total of 24 pull-out specimens were fabricated, with three replicates for each combination of bonded length and number of WD cycles. The specimen designation and test matrix are summarized in Table 6. For instance, S-L40-WD30 denotes specimens with 40 mm bonded length, and subjected to 30 WD cycles. While three replicates per test group are consistent with many bond durability studies, it should be acknowledged that this limited sample size may increase the influence of specimen-to-specimen variability on the measured results, particularly for bond parameters such as residual bond strength and bond stiffness.

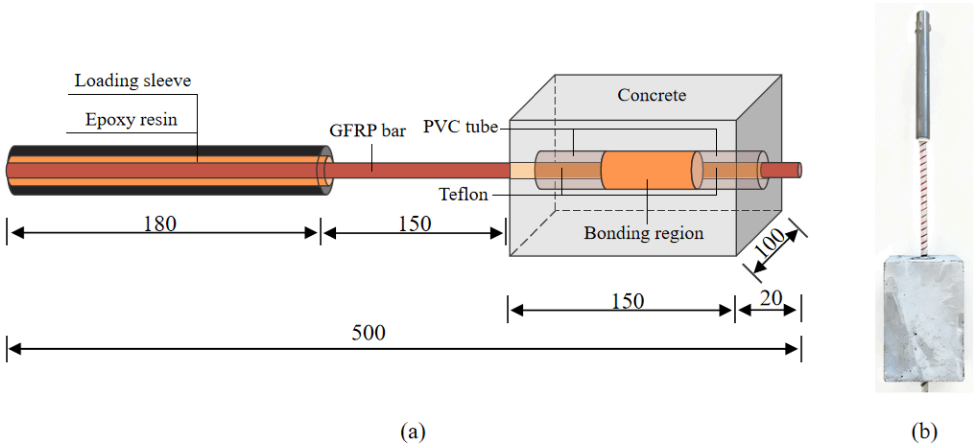

Figure 4. Pull-out specimens (dimensions in mm): (**a**) schematic diagram; and (**b**) test sample.

Table 6. Summary of pull-out test specimens.

Specimen ID	Number of WD Cycles	Bonded Length (mm)	Replicated Samples
S-L40-WD00	0	40	3
S-L40-WD30	30	40	3
S-L40-WD60	60	40	3
S-L40-WD90	90	40	3
S-L80-WD00	0	80	3
S-L80-WD30	30	80	3
S-L80-WD60	60	80	3
S-L80-WD90	90	80	3

2.3. Wetting–Drying Cycle Exposure

For each pull-out specimen, WD cycling tests were conducted using a TR-LS sulfate corrosion testing apparatus, produced by Tongrui Instrument Equipment Co., Ltd., Shanghai, China, according to the Chinese standard GB/T 50082-2024 [35]. After 28 days of standard curing, the specimens were subjected to WD cycles in artificial seawater. Each complete WD cycle lasted 24 h and consisted of the following phases, as specified in Ref. [35]:

(i) Immersion (15 h): The chamber was filled with artificial seawater at 25 °C until the specimens were submerged by 20 mm. Immersion lasted for 15 h.
(ii) Drainage and air-drying (1 h): The solution was drained, and specimens were air-dried at ambient temperature for 1 h.
(iii) Heating and drying (6 h): The chamber temperature was raised to 40 °C, and specimens were dried for 6 h.
(iv) Cooling (2 h): The chamber was cooled to 25 °C over 2 h.

Before the start of WD cycling, all specimens were taken directly from the standard curing room without any pre-drying treatment. Each complete WD cycle lasted 24 h and consisted of the following phases as specified in GB/T 50082-2024 [35]. Immersion phase lasted 15 h, during which the chamber was filled with artificial seawater at 25 °C until the specimens were submerged by 20 mm. Drainage and air-drying followed for 1 h, during which the solution was drained and the specimens were air-dried at ambient temperature. The heating and drying phase was then conducted at 40 °C for 6 h. Finally, the chamber was cooled to 25 °C over 2 h. The artificial seawater was replaced monthly to maintain its chemical composition.

Upon completion of the target number of cycles (30, 60, or 90), the specimens were removed from the chamber and allowed to equilibrate in the laboratory environment at 23 ± 2 °C and 50 ± 5% relative humidity for 2 h. After this equilibration period, any visible surface water was gently wiped with a dry cloth, resulting in a surface-dry condition at the time of pull-out testing. No visible salt crystallization was observed on any specimen surfaces, even after 90 cycles, which is attributed to the monthly replacement of the artificial seawater. Concrete surfaces showed no spalling or cracking, and only slight discoloration of the exposed epoxy adhesive was noted. Mass change in specimens was not recorded, as the primary objective of this study was the bond performance rather than mass transport properties. The described protocol ensures reproducibility of the WD exposure. The complete specimen fabrication and WD cycle exposure process is illustrated in Figure 5.

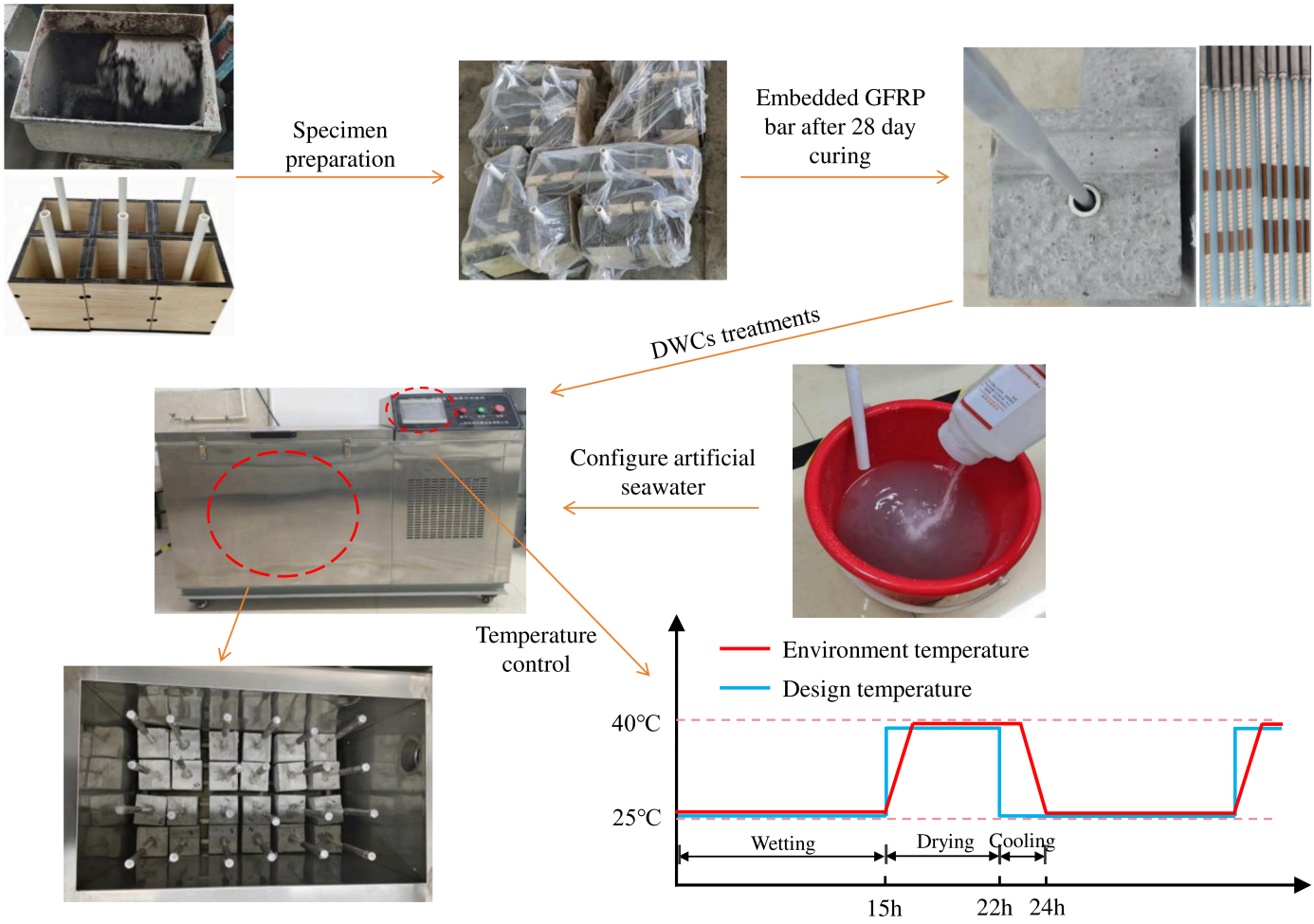

Figure 5. Specimen fabrication and WD cycle exposure process.

Ninety WD cycles, each lasting 24 h, correspond to 90 days of continuous accelerated testing. This duration is commonly used in laboratory studies to simulate the early stage of bond degradation in tidal and splash zones, although it does not directly translate to a specific number of years of field service due to variations in environmental severity and material response. The selection of 90 WD cycles as the maximum exposure in this study is consistent with the typical range adopted in the literature for EB and NSM FRP–concrete bond durability under WD environments. For instance, Gong et al. [27] investigated the bond behavior of NSM CFRP-to-concrete joints under chloride WD cycles with a maximum of 90 cycles. Cui et al. [20] and Song et al. [36] studied the bond degradation of EB CFRP-to-concrete interfaces with and without surface grooves under WD cycles with a maximum of 120 days (approximately 120 cycles). However, 90 days of accelerated testing is far shorter than the design service life of marine structures. A long-term study by Hao et al. [37] investigated the bond durability of EB FRP-to-concrete joints subjected to 110 months (approximately 3300 cycles) of combined accelerated laboratory and field exposure. Their results showed that the bond degradation continued beyond 90 cycles but at a decreasing rate. Notably, for certain CFRP–adhesive combinations (CFRP plate with Sika30 and CFRP sheet with SW-3C), the reductions in the bond strength after 110 months were only 2% and 9%, respectively [37]. This finding indicates that while the 90-cycle program in this study captures the early rapid degradation phase, extrapolation to decades of service life is not directly possible. Therefore, the present results should be interpreted as an initial quantification of bond degradation under moderate WD exposure, and longer-term

cycling (e.g., up to 360 or more cycles) is needed to fully characterize the long-term bond performance of GFRP adhesive anchors in concrete.

2.4. Pull-Out Test Setup

After completing the designated number of WD cycles, pull-out tests were conducted via the WAW-1000B electro-hydraulic servo universal testing machine (manufactured by Keda Testing Machine Manufacturing Co., Ltd., Changchun, China) equipped with a custom-built reaction frame, as shown in Figure 6. Displacement-controlled monotonic loading was applied at a rate of 0.03 mm/s. The applied load was recorded directly by the testing machine's internal load cell. The load-end slip of the GFRP bar was measured using a high-precision linear variable displacement transducer (LVDT) and a data acquisition system with a sampling frequency of 10 Hz. It should be noted that the displacement measured by the LVDT comprises not only the actual bond slip but also the elastic elongation of the unbonded segment of the GFRP bar extending from the loaded end to the concrete surface. Owing to the relatively low elastic modulus of GFRP, this elongation contributes significantly to the measured value and cannot be neglected. Therefore, the true slip (s) was determined by subtracting the elastic elongation from the total measured displacement (s_m), following the method described in [10].

$$s = s_m - \Delta_{elongation} \text{ where } \Delta_{bar,\ elongation} = \frac{F \cdot L_f}{A_s \cdot E_t}, \quad (1)$$

where F = applied force; s = actual slip; s_m = displacement recorded by transducer; $\Delta_{elongation}$ = elastic elongation of the free length of the bar; A_s = cross-sectional area of the bar; and E_t = elastic modulus of the bar. The bond stress τ_b is calculated from the measured force as:

$$\tau_b = \frac{F}{\pi d_b L_b}, \quad (2)$$

where L_b = bonded length; and d_b = bar diameter.

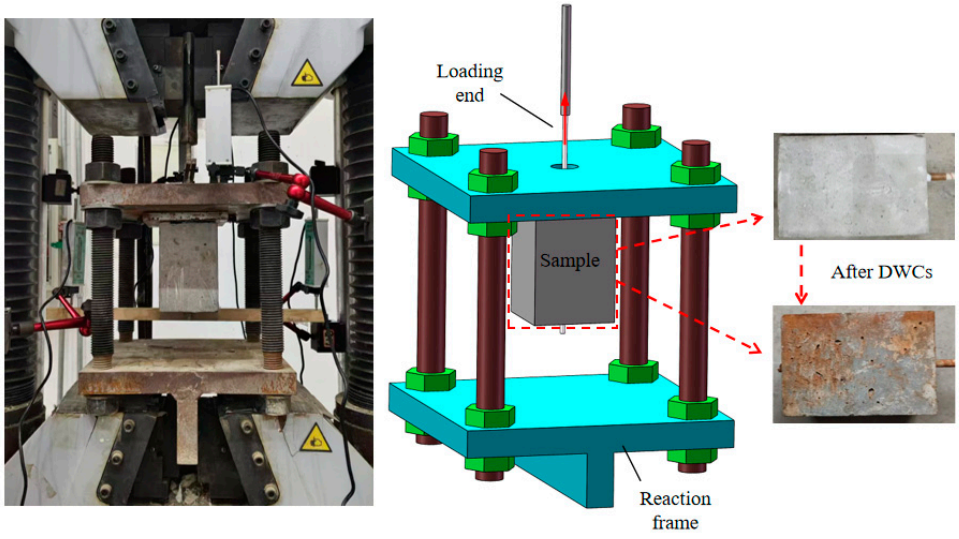

Figure 6. Pull-out tests after WD cycles.

3. Experimental Results and Discussion

3.1. Failure Mode

All pull-out specimens were failed by the pull-out of GFRP bars, characterized by debonding at the interface, as shown in Figure 7. No concrete splitting or bar rupture was observed throughout the tests, attributable to the adequate concrete cover and the relatively

low bond strength of sand-coated GFRP bars compared to ribbed steel bars. Despite the consistent pull-out failure mode, the number of WD cycles exhibited a significant influence on the failure pattern at the GFRP–adhesive–concrete interface.

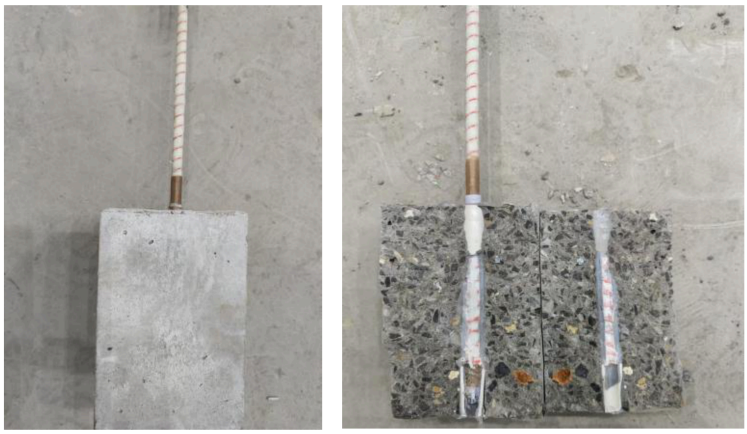

Figure 7. Bar pull-out failure due to slippage between GFRP bar and concrete. The concrete in the right image was deliberately split after the pull-out test to expose the bonded interface for failure mode observation, and no concrete splitting occurred during the test.

In the absence of WD exposure (0 cycles), failure occurred predominantly at the bar–adhesive interface, characterized by debonding of the sand-coated layer from the bar surface. The sand coating was completely stripped off, leaving a relatively smooth bar surface, while the epoxy adhesive remained largely intact and bonded to the concrete, with visible splitting cracks within the adhesive layer. This indicates that the bond between the adhesive and concrete was stronger than the bond between the adhesive and the sand-coated bar surface. The rough sand coating generated significant radial dilation stresses during pull-out, leading to circumferential tensile stresses that caused splitting of the adhesive.

After 30 WD cycles, the primary failure remained at the bar–adhesive interface with sand coating debonding. However, the first signs of degradation at the adhesive–concrete interface became observable. The hydration products at the interfacial transition zone (ITZ) of concrete softened due to moisture ingress and ion exchange, leading to localized detachment of fine aggregate particles that adhered to the adhesive surface. Compared to the unexposed control specimens (0 cycles), the adhesive layer exhibited fewer and narrower splitting cracks, suggesting reduced radial dilation due to softening of the GFRP resin matrix and the sand coating layer.

After 60 WD cycles, the damage became more severe. Significant portions of the adhesive–concrete interface exhibited debonding, with mortar particles from the concrete substrate visibly attached to the adhesive surface. The adhesive showed only minor splitting cracks. This shift in the failure mode indicates that the adhesive–concrete interface had become substantially weakened by the cyclic exposure, making it more susceptible to failure. The bar surface showed signs of resin softening and discoloration, further reducing the mechanical interlock provided by the sand coating.

After 90 WD cycles, the adhesive remained largely intact with minimal splitting, but extensive debonding occurred at the adhesive–concrete interface, with only a thin layer of cement paste detached from the concrete substrate adhering to the adhesive. The bar surface exhibited noticeable deterioration, including resin softening and slight surface roughening. This failure mode progression highlights a gradual shift from adhesive–bar interface bond failure toward adhesive–concrete bond interface failure as the number of WD cycles increases.

This progressive shift in the failure mode is attributed to three coupled degradation mechanisms induced by WD cycling, i.e., degradations of the adhesive, the ITZ of concrete, and the GFRP bar surface (interface between the sand coating and the bar core). A quantitative assessment of the change in the failure mode was performed by counting the number of specimens exhibiting each dominant failure interface at each WD cycle level. At 0 cycles, all three replicate specimens (100%) failed at the bar–adhesive interface with no visible adhesive–concrete debonding. After 30 cycles, two out of three specimens (67%) still showed bar–adhesive failure as the dominant mode, while one specimen (33%) exhibited partial debonding at the adhesive–concrete interface. After 60 cycles, the dominant failure mode was mixed. That is, two specimens (67%) showed involvement of both interfaces, and one specimen (33%) failed primarily at the adhesive–concrete interface. After 90 cycles, all three specimens (100%) failed predominantly at the adhesive–concrete interface, with the bar–adhesive interface remaining largely intact. This quantitative progression in the failure mode confirms that the critical interface shifts from bar–adhesive to adhesive–concrete as the number of WD cycles increases. Further microscopic analysis would be an advantage to support the obtained results and this will be investigated in our future studies.

3.2. Bond Stress–Slip Curves

The bond stress versus slip curves for all tested specimens are shown in Figure 8. It was found that all these curves exhibit a consistent three-stage shape, comprising an ascending branch, a descending branch, and a residual frictional branch, regardless of the bonded length or number of WD cycles. This characteristic shape reflects the progressive damage and failure process at the GFRP–adhesive–concrete interface. The initial bond stiffness K_t is defined as the slope of the ascending branch of the bond stress–slip curve. It is computed by linear regression over the data points between 25% and 50% of the peak bond stress τ_{bmax}, following the method proposed by Rosa et al. [38] for sand-coated GFRP bars. This range was selected because it represents the linear elastic response before significant local damage accumulation at the interface. The residual bond stress τ_{br} is defined as the bond stress at the end of the descending branch, after which the bond stress falls to a residual frictional level and stabilizes with minor fluctuations during continued bar slip. These minor fluctuations are governed by a stick–slip mechanism arising from the interaction between the FRP bar surface (e.g., sand coating or ribs) and the surrounding adhesive. During post-debonding slip, the surface features of the bar engage in sequence. Each feature alternately grips the adhesive and then breaks free, producing oscillatory shear stress through a stick–slip mechanism. This interpretation is consistent with the findings of Refs. [38,39] on the post-peak bond behavior of sand-coated FRP bars.

Specifically, both $\tau_{b\max}$ and K_t decreased significantly with increasing WD cycles, indicating progressive degradation of the interfacial bond resistance. This reduction could be attributed to the cumulative damage inflicted by cyclic environmental exposure, which weakens the adhesive, the concrete ITZ, and the GFRP bar surface, as discussed in Section 3.1. From a theoretical perspective, the bond mechanism in sand-coated GFRP bars relies on three components: chemical adhesion, mechanical interlock provided by the sand coating, and friction [39]. However, each of these components was damaged due to the presence of WD exposure damage in each of these components, i.e., chemical bonds are hydrolyzed, the sand coating loses its interlocking capacity due to resin softening, and frictional resistance diminishes as the interfaces become smoother and debris accumulates. During the residual stage, the interface retained a certain bond stress (τ_{br}) against slip and experienced slight stress fluctuations. As shown in Figure 8, the residual bond stress caused by friction reduced with the increase in WD cycles, regardless of the bonded length. Table 7

summarizes the experimental results of the bond strength, the residual bond strength, and the bond stiffness under different WD cycles and bonded lengths.

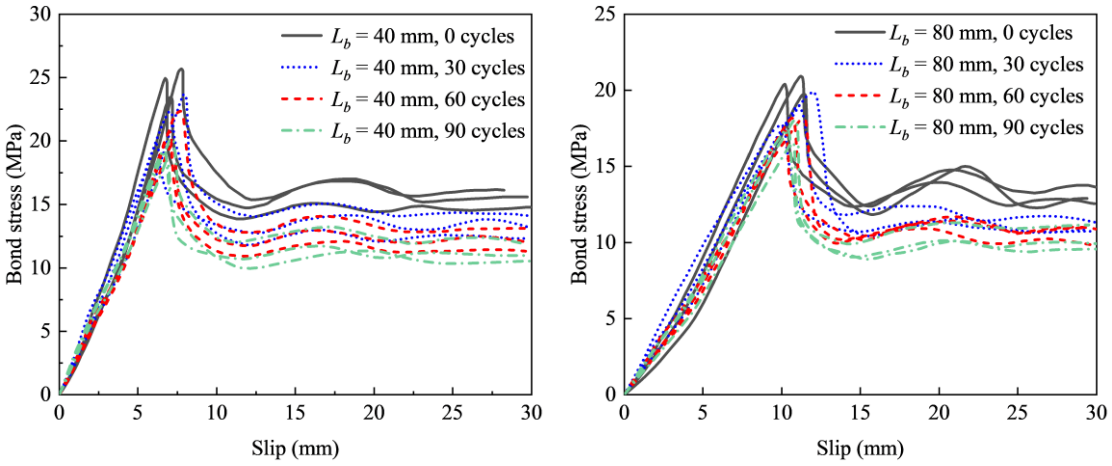

(a) Bonded length L_b = 40 mm (b) Bonded length L_b = 80 mm

Figure 8. Bond stress–slip curves under different WD cycles for specimens with (**a**) bonded length of 40 mm (5 times the bar diameter) and (**b**) bonded length of 80 mm (10 times the bar diameter). Each curve is representative of three replicate specimens. Distinct line patterns are used to differentiate the number of WD cycles: solid line for 0 cycles, dotted line for 30 cycles, dashed line for 60 cycles, and dash–dot line for 90 cycles. The legend entries indicate both the bonded length and the cycle number (e.g., "L = 40 mm, 0 cycles").

Table 7. Summary of pull-out test results for all specimen groups with 95% confidence intervals (CI) for t_{bmax}, t_{br}, and K_t.

Specimen ID	τ_{bmax} (MPa)	95% CI for τ_{bmax}	τ_{br} (MPa)	95% CI for τ_{br}	K_t (MPa/mm)	95% CI for K_t
S-L40-WD00	24.68 ± 1.13	(21.87, 26.49)	14.64 ± 0.75	(12.78, 16.50)	3.45 ± 0.22	(3.01, 3.89)
S-L40-WD30	21.94 ± 2.01	(18.94, 24.94)	12.86 ± 1.11	(10.10, 15.62)	3.13 ± 0.13	(2.88, 3.38)
S-L40-WD60	20.91 ± 1.36	(17.53, 24.29)	11.84 ± 0.94	(9.50, 14.18)	2.87 ± 0.11	(2.67, 3.07)
S-L40-WD90	19.28 ± 0.91	(17.02, 21.54)	10.90 ± 1.05	(8.29, 13.51)	2.80 ± 0.10	(2.62, 2.98)
S-L80-WD00	20.35 ± 0.59	(18.88, 21.82)	12.19 ± 0.31	(11.42, 12.96)	1.87 ± 0.14	(1.61, 2.13)
S-L80-WD30	18.69 ± 1.09	(15.99, 21.39)	10.99 ± 0.73	(9.18, 12.80)	1.72 ± 0.05	(1.63, 1.81)
S-L80-WD60	17.61 ± 0.48	(16.42, 18.80)	10.10 ± 0.12	(9.80, 10.40)	1.67 ± 0.07	(1.54, 1.80)
S-L80-WD90	17.36 ± 0.73	(15.55, 19.17)	9.28 ± 0.55	(7.92, 10.64)	1.64 ± 0.07	(1.51, 1.77)

Notes: τ_{bmax} = maximum bond stress; τ_{br} = residual bond stress; and K_t = initial bond stiffness. These values are presented as mean ± standard deviation; 95% CI were calculated using the t-distribution with 2 degrees of freedom (t = 4.303).

To verify that the observed bond strength reductions are statistically significant, a one-way analysis of variance (ANOVA) was performed for each bonded length group. The null hypothesis was that the mean bond strengths at 0, 30, 60, and 90 WD cycles are equal. For the 40 mm bonded length, the calculated F-value was 8.67 with a *p*-value of 0.003; for the 80 mm bonded length, the F-value was 5.92 with a *p*-value of 0.012. Since both *p*-values are below 0.05, the null hypothesis is rejected, confirming that the WD cycles have a statistically significant effect on bond strength degradation. Post hoc Tukey tests further indicated that the reductions between 0 and 30 cycles and between 30 and 60 cycles are significant, while the reduction between 60 and 90 cycles is not statistically significant

($p > 0.05$). This supports the nonlinear degradation pattern characterized by rapid initial degradation followed by a gradual stabilization.

The failure process under WD exposure evolves through three distinct debonding stages, as schematically illustrated in Figure 9. It follows that:

(i) Ascending stage (OA): In the pre-peak stage, the response is nearly linear until τ_{bmax} is reached. This stage is governed primarily by chemical adhesion and interlock between the sand coating and the epoxy adhesive. Micro-damage initiates at the interface but remains localized. The bond stiffness K_t, defined as the slope of this branch, decreases progressively with increasing WD cycles, reflecting the cumulative interfacial damage prior to loading.

(ii) Descending stage (AB): After reaching the peak, the bond stress declines as damage propagates rapidly along the bonded interface. For unexposed specimens, this drop is steep, corresponding to sudden debonding of the sand coating. For specimens subjected to WD cycles, the descending branch becomes more gradual, indicating a more progressive failure mode as multiple interfaces (bar–adhesive and adhesive–concrete) contribute to the damage process. The sand coating is partially sheared off, and the adhesive–concrete interface begins to separate.

(iii) Residual stage (BC): As the bond stress decreases to the residual stress τ_{br}, it stabilizes with minor fluctuations as the bar continues to slip. This residual resistance is contributed primarily by friction between bar surfaces (with remnants of sand coating) and the damaged adhesive or concrete debris. The magnitude of τ_{br} decreases with increasing cycles, while the amplitude of fluctuations also remains unchanged. This confirms the progressive smoothing of interacting surfaces and reduction in frictional resistance.

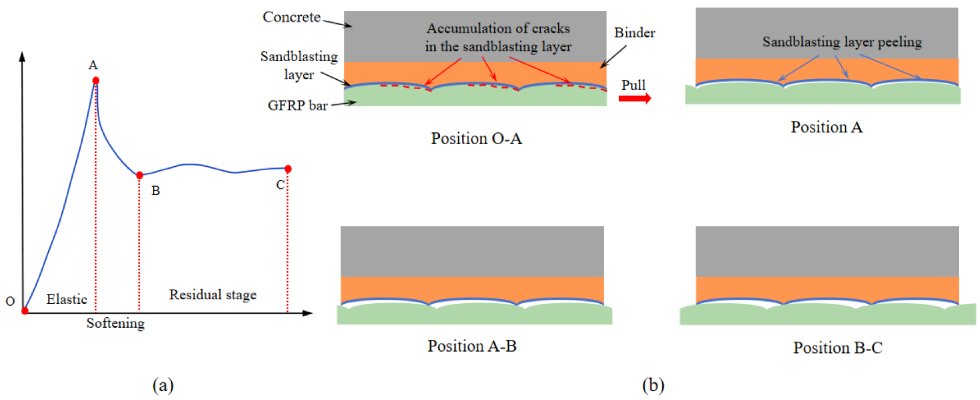

Figure 9. Schematic illustration of (**a**) the simplified bond–slip curve and (**b**) failure process.

3.3. Bond Strength

3.3.1. Influence of WD Cycles on Bond Strength

Figure 10 plots the average bond strength values against the number of WD cycles. As anticipated, both the bond strength and the residual bond strength at the interface decreased progressively with increasing WD cycles, although the degradation was less severe than that observed in freeze–thaw studies due to the milder nature of WD exposure compared to freeze–thaw exposure [40]. Specifically, for L40 specimens, the bond strength decreased from 24.68 MPa at 0 cycles to 21.94 MPa at 30 cycles (11.10% loss), 20.91 MPa at 60 cycles (15.28% loss), and 19.28 MPa at 90 cycles (21.87% loss). For L80 specimens, the corresponding values decreased from 20.35 MPa at 0 cycles to 18.69 MPa at 30 cycles (8.16% loss), 17.61 MPa at 60 cycles (13.46% loss), and 17.36 MPa at 90 cycles (14.72% loss).

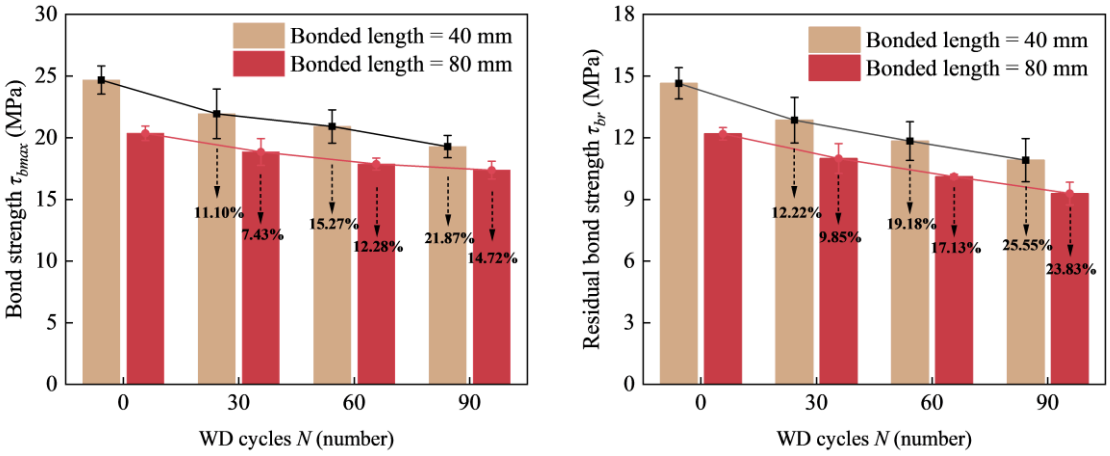

(a) Bond strength (b) Residual bond strength

Figure 10. Effect of WD cycles on (**a**) bond strength and (**b**) residual bond strength. Error bars indicate one standard deviation calculated from three replicate specimens. The legend distinguishes the two bonded lengths: "Bonded length = 40 mm" and "Bonded length = 80 mm".

Notably, several observations can be made from these experimental results. First, the bond strength degradation followed a nonlinear trend rather than a simple linear one, with the most pronounced decrease occurring within the first 30 cycles, after which the degradation rate gradually slowed, as shown in Figure 10a. This trend mirrors the degradation pattern of the concrete substrate and adhesive under cyclic WD exposure, where initial rapid interfacial bond damage accumulation (microcracking and hydrolysis) is followed by a stabilization phase as damage approaches a saturation point. Second, as shown in Table 5, the residual bond strength underwent an even more severe reduction compared to the bond strength. To be more specific, for L40 specimens, the residual bond strength decreased from 14.64 MPa at 0 cycles to 10.90 MPa at 90 cycles (25.55% loss). For L80 specimens, it decreased from 12.19 MPa to 9.28 MPa (23.83% loss). This makes sense both theoretically and practically as the residual capacity is primarily provided by friction and the mechanical interlock of damaged interfaces, which are highly sensitive to the accumulated damage from WD cycles. With increasing cycles, the post-peak stress fluctuations became less pronounced, further indicating the diminished contribution of mechanical interlock in the residual stage, as demonstrated in Figure 10b.

3.3.2. Influence of Bonded Length on Bond Strength

Figure 11 compares the bond strength values of L40 and L80 specimens under different numbers of WD cycles. As expected, increasing the bonded length from 40 mm (five times the anchor diameter) to 80 mm (10 times the anchor diameter) resulted in a marked decrease in both the peak and residual bond strength values, regardless of the number of WD cycles. Taking the bond strength t_{bmax} as an example, at 0 cycles, t_{bmax} was 24.68 MPa for L40 specimens but only 20.35 MPa for L80 specimens (a 17.52% reduction). Similar reductions were observed at 30 cycles (14.12%), 60 cycles (14.61%), and 90 cycles (9.97%). The reason can be elaborated as follows.

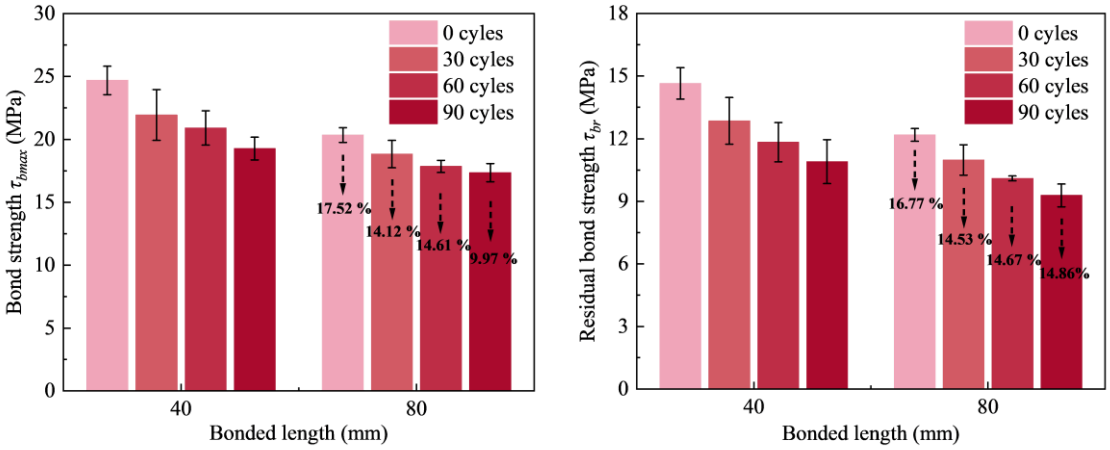

(a) Bond strength (b) Residual bond strength

Figure 11. Effect of bonded length on (**a**) bond strength and (**b**) residual bond strength. Error bars indicate one standard deviation calculated from three replicate specimens. The legend shows the four WD cycle levels: "0 cycles", "30 cycles", "60 cycles", and "90 cycles".

As the bonded length increases, the bond stress distribution along the bonded region becomes more significant. This phenomenon is well-documented in bond–slip studies of FRP bars [40]. For shorter bonded lengths, the bond stress distribution is more uniform, allowing the entire bonded region to contribute more effectively to resisting pull-out. As the bonded length increases, stress concentration at the loaded end becomes more pronounced, while the far end remains understressed. Consequently, the average bond stress at failure, i.e., t_{bmax}, decreases with increasing bonded length. This interesting effect is captured by the nonlinear relationship between the pull-out force and bonded area. While L80 specimens had twice the bonded area of L40 specimens, the maximum pull-out force $P_{\max}$ was only 1.65 times higher at 0 cycles, reflecting this non-uniformity.

It is interesting to note that although L80 specimens had lower absolute bond strength values, they exhibited superior durability with lower strength loss percentages. For instance, at 90 cycles, L40 specimens lost 21.87% of their initial bond strength, while L80 specimens lost only 14.72%. This enhanced durability can be explained by the so-called "reserve length" effect. In longer bonded length cases, the bonded region near the loaded end experiences the most severe environmental attack and highest stress concentration. The bonded region further from the loaded end, however, is protected from severe deterioration due to lower stress levels. As the loaded end progressively degrades under WD cycles, the undamaged bonded portion can still provide significant bond resistance. In contrast, for short bonded lengths, the entire bonded region is directly exposed to environmental attack and stress concentration, leading to more uniform but more severe bond degradation. This mechanism is analogous to the "size effect" phenomenon observed in durability studies of externally bonded FRP-to-concrete joints [41].

Despite this, the difference in bond strength between L40 and L80 specimens decreased with increasing WD cycles, from 4.33 MPa at 0 cycles to 1.92 MPa at 90 cycles. This convergence suggests that under severe environmental exposure, the influence of bonded length on bond strength diminishes as the interface becomes progressively damaged throughout the entire bonded length. The practical implication of these findings is that while longer bonded lengths provide lower nominal bond strength in the short term, they offer enhanced durability and more predictable long-term performance in marine environments. This may be helpful in the bonded length design of GFRP anchors in coastal infrastructure where long-term reliability is paramount.

3.4. Interfacial Damage Mechanism Under WD Cycles

The observed bond degradation under WD cycles can be interpreted through three coupled mechanisms documented in previous studies on EB and NSM FRP systems [18,20]. First, the epoxy adhesive layer undergoes hydrolysis and plasticization due to moisture ingress. As reported by Wang et al. [18], the tensile strength and elastic modulus of the adhesive under salt solution WD cycles decreased substantially, and brittle fracture became more pronounced. This chemical degradation directly weakens the adhesive bulk phase and both interfaces (bar–adhesive and adhesive–concrete). Second, the interfacial transition zone (ITZ) of concrete is attacked by chloride ions, resulting in softening of calcium–silicate–hydrate gels and the formation of expansive products that generate microcracks. Third, the resin matrix on the GFRP bar surface experiences osmotic cracking, compromising the sand coating and reducing mechanical interlock forces.

Specifically, the progressive shift in the failure mode from the bar–adhesive interface to the adhesive–concrete interface with increasing WD cycles observed in this study is consistent with the mechanism described by Zeng et al. [26] for a GFRP bar-to-concrete bond. In their study on GFRP bars embedded in ultra-high-strength concrete, two distinct failure mechanisms were identified: shear failure between concrete and the outer resin surface, and shear failure between the bar fiber and the resin. In this study, the adhesive layer becomes the weakest link under WD cycles, causing the failure to shift from the bar–adhesive interface to the adhesive–concrete interface. This phenomenon has not been previously documented for ETS systems but is consistent with the general understanding that moisture preferentially attacks the adhesive layer. Comparison with existing studies on bond degradation in other FRP systems further supports the mechanistic interpretation. Wang et al. [18] and Gong et al. [27] reported that both the EB and NSM CFRP-to-concrete interfaces also exhibited a nonlinear degradation pattern with rapid initial loss followed by stabilization. The same degradation law is observed in the ETS FRP bar-to-concrete interface, suggesting a common underlying damage process. However, the ETS FRP systems show lower absolute bond strength degradation due to their larger concrete cover, which will be discussed quantitatively in Section 4.2. The mechanistic understanding derived here provides a rigorous basis for the bond strength model developed later.

4. Analytical Modeling of Bond Strength Degradation

Accurate prediction of bond strength degradation under WD cycles constitutes a fundamental requirement for the durability-based design of GFRP adhesive anchor systems deployed in marine environments. However, current design codes and guidelines, exemplified by ACI 440.3R-15 [42], predominantly focus on the material deterioration of FRP bars themselves while offering limited guidance on the degradation of bond performance at the bar-to-concrete interface. Moreover, although extensive research has examined the bond behavior of FRP reinforcements subjected to various environmental exposure, generalized models enabling quantitative prediction of bond degradation arising from the coupled effects of WD cycles and bonded length remain scarce. To address this gap, this section presents empirically derived models developed to simulate the bond strength degradation of GFRP adhesive anchors under WD cycles, with explicit incorporation of bonded length as a key influencing parameter.

4.1. Model Formulation

For sand-coated GFRP bars, their bond mechanism relies primarily on mechanical interlock provided by the sand particles and chemical adhesion between the adhesive and

the bar surface [43]. A commonly accepted form for bond strength models at ambient temperature, as adopted in previous studies [42,44], can be expressed as:

$$\frac{\tau_{b\max,0}}{f_{cu,0}} = \alpha_1 + \alpha_2 \frac{c}{d_b} + \alpha_3 \frac{L_b}{d_b}, \tag{3}$$

where $\tau_{b\max,0}$ is the bond strength at 0 WD cycles; $f_{cu,0}$ is the undegraded concrete compressive strength at 28 days (53.96 MPa); L_b/d_b represents the relative bonded length (ratio of bonded length to bar diameter); c refers to the concrete cover; and α_1, α_2, and α_3 are dimensionless coefficients to be determined through regression analysis. In this study, the bar diameter (d_b = 8 mm) and concrete cover (c = 46 mm) were kept constant for all specimens, resulting in a constant relative cover ratio of c/d_b = 5.75. For this special case, Equation (3) can be reduced to:

$$\frac{\tau_{b\max,0}}{f_{cu,0}} = A + \alpha_3 \frac{L_b}{d_b}, \tag{4}$$

where $A = \alpha_1 + \alpha_2 \frac{c}{d_b}$ refers to a combined constant that incorporates the effect of concrete cover.

To incorporate the degradation effects induced by WD cycles, a cycle-dependent reduction factor, denoted as $\eta(N)$, is introduced, where N is the number of WD cycles. This approach is consistent with established methodologies for modeling bond degradation under elevated temperatures [11,44], where a reduction factor is employed to the ambient-condition bond strength to account for progressive deterioration. Accordingly, the reduction factor $\eta(N)$ quantifies the remaining bond strength fraction after N WD cycles and can be defined as:

$$\eta(N) = \frac{\tau_{b\max,N}}{\tau_{b\max,0}}, \tag{5}$$

where $\tau_{b\max,N}$ is the bond strength after N WD cycles. Figures 12a and 12b show the normalized peak and residual bond strengths as a function of N, respectively.

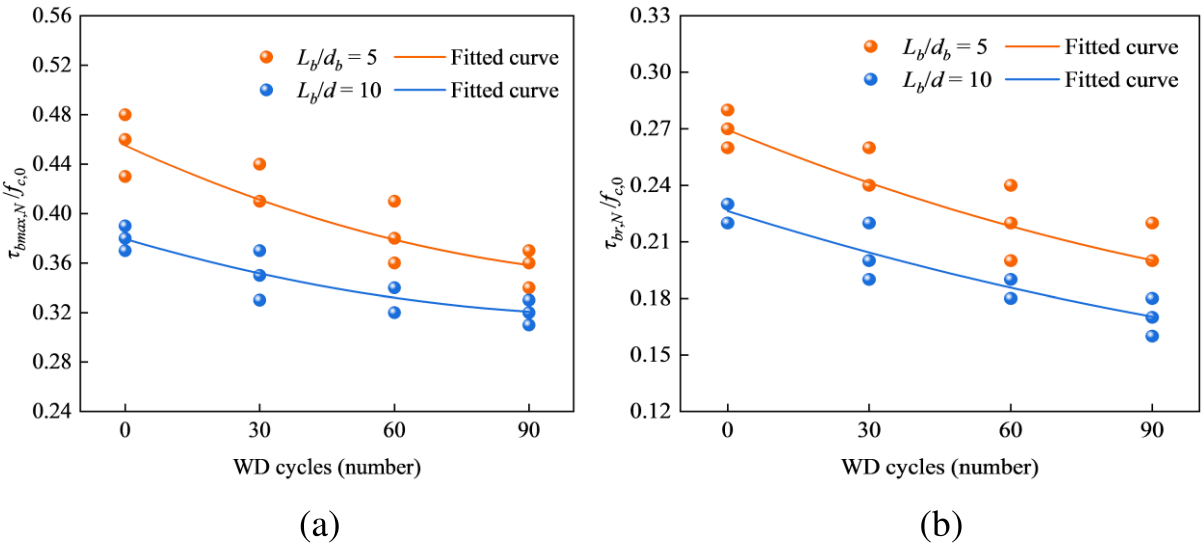

Figure 12. Normalized values of (**a**) bond strength and (**b**) residual bond strength as a function of number of WD cycles. Each data point represents an individual specimen (all three replicates per test group are shown). Error bars are not presented because the raw individual data are plotted directly. The fitted curves show good agreement with the test results, with correlation coefficients of 0.95.

According to Figure 12, the degradation of the bond strength follows a nonlinear trend with increasing WD cycles, with the most pronounced reduction occurring within the first

30 cycles. Furthermore, the degradation rate is influenced by the bond length, with longer bonded lengths exhibiting enhanced durability (i.e., lower degradation rates). To capture these coupled effects, a second-order polynomial function of N is proposed for $\eta(N)$, with coefficients that depend on the relative bond length L_b/d_b:

$$\eta(N) = a_u(L_b/d_b) \cdot N + b_u(L_b/d_b) \cdot N^2 + 1, \tag{6}$$

where $a_u(L_b/d_b)$ and $b_u(L_b/d_b)$ are functions of the relative bonded length that can be determined from regression analysis. Although the bond degradation trend exhibits a rapid initial decline followed by gradual stabilization, which might suggest a logarithmic relationship, a logarithmic transformation of the cycle number N was not adopted. Herein, the quadratic polynomial function of N is selected because it provides a simple yet accurate fit to the experimental data (correlation coefficients above 0.95 in Figure 12) and is more convenient for engineering design than a logarithmic model. This functional form is also commonly used in modeling the environmental degradation of the FRP bar-to-concrete bond [11].

4.2. Parameter Calibration and Model Validation

Multi-variable nonlinear regression analysis was performed using the experimental data presented in Table 5 (see Section 3.3) to calibrate the unknown coefficients in Equations (4) and (6). The analysis followed a sequential approach. First, the ambient-condition coefficients (α_1, α_2, and α_3) were obtained using the 0-cycle data. Subsequently, the cycle-dependent coefficients were calibrated for each bond length group. Finally, the functional relationships between these coefficients and L_b/d_b were established.

Based on the test results for specimens exposed to 0 WD cycles, i.e., Specimens S-L40-WD00 and S-L80-WD00, the normalized bond strengths $\frac{\tau_{b\max,0}}{f_{cu,0}}$ were calculated as:

$$\frac{\tau_{b\max,0}}{f_{cu,0}} = (24.68/53.96) = 0.4575 \text{ for } L_b/d_b = 5, \tag{7a}$$

$$\frac{\tau_{b\max,0}}{f_{cu,0}} = (20.35/53.96) = 0.3771 \text{ for } L_b/d_b = 10. \tag{7b}$$

Substituting Equation (7a,b) into Equation (4) and using the linear regression of these two data points, it follows that:

$$A = 0.5379 \text{ and } k_3 = -0.01608. \tag{8}$$

The bond strength model under ambient condition then becomes:

$$\frac{\tau_{b\max,0}}{f_{cu,0}} = 0.5379 - 0.01608 \cdot \frac{L_d}{d_b} \text{ or } \tau_{b\max,0} = f_{cu,0} \cdot \left(0.5379 - 0.01608 \cdot \frac{L_d}{d_b}\right). \tag{9}$$

The negative coefficient for the relative bond length (L_d/d_b) presented in Equation (9) confirms the inverse relationship between the bonded length and the nominal bond strength discussed in Section 3.4, reflecting the non-uniform distribution of bond stress along longer bonded lengths [45]. The constant term A = 0.5379 implicitly incorporates the effect of the constant concrete cover ratio.

For the WD cycle-dependent reduction factor, the normalized bond strength ratios $\eta(N)$ were computed for each bonded length group using experimentally measured $\tau_{b\max,0}$. Quadratic regression of $\eta(N)$ against N led to:

$$a_u(5) = -0.00616 \text{ and } b_u(5) = 2.29 \times 10^{-5} \text{ for } L_b/d_b = 5, \tag{10a}$$

$$a_u(10) = -0.00851 \text{ and } b_u(10) = 3.13 \times 10^{-5} \text{ for } L_b/d_b = 10. \quad (10b)$$

Thus, these coefficients were linearly correlated with L_b/d_b to give:

$$a_u\left(\frac{L_d}{d_b}\right) = -0.00381 - 0.00047 \cdot \frac{L_d}{d_b}, \quad (11a)$$

$$b_u\left(\frac{L_d}{d_b}\right) = 2.15 \times 10^{-5} + 2.83 \times 10^{-6} \cdot \frac{L_d}{d_b}. \quad (11b)$$

Combining Equation (11a,b) with Equations (5) and (6) leads to the complete expression for the bond strength after N WD cycles:

$$\tau_{b\max,N} = \tau_{b\max,0} \cdot \left[1 + \left(-0.00381 - 0.00047\frac{L_d}{d_b}\right)N + \left(2.15 \times 10^{-5} + 2.83 \times 10^{-6}\frac{L_d}{d_b}\right)N^2\right] \quad (12)$$

where the expression for $\tau_{b\max,0}$ has been given by Equation (9), or equivalently:

$$\tau_{b\max,N} = f_{cu,0}\left(0.5379 - 0.01608\frac{L_d}{d_b}\right)\left[1 - \left(0.00381 + 0.00047\frac{L_d}{d_b}\right)N + \left(2.15 \times 10^{-5} + 2.83 \times 10^{-6}\frac{L_d}{d_b}\right)N^2\right] \quad (13)$$

A key advantage of the bond strength degradation equation presented in Equation (13) is its practical simplicity. Given only the undegraded concrete compressive strength $f_{cu,0}$, the bond strength after N WD cycles for any relative bond length ($\frac{L_d}{d_b}$) can be directly calculated. This eliminates the need for measuring degraded material properties, which represents a significant practical benefit for engineering applications.

It is important to clarify that the model presented in Equations (12) and (13) was calibrated using the experimental data from this study. Therefore, Figure 13 represents a goodness of fit rather than an independent validation. To assess the internal robustness of the model, a leave-one-bonded-length-out cross-validation was performed. The model was calibrated using only the data from specimens with a bonded length of 40 mm to predict the bond strength of specimens with a bonded length of 80 mm, and vice versa. The mean absolute percentage error (MAPE) for cross-validation predictions was 11.7% when predicting the 80 mm bonded length specimens from the 40 mm data and 9.8% when predicting the 40 mm bonded length specimens from the 80 mm data. These errors are within acceptable limits for engineering applications, confirming that the model captures the bonded length effect without overfitting.

A direct comparison with existing models and design guidelines is necessary to position the contribution of this work. The current ACI 440.3R-15 guideline [42] provides provisions for testing the material deterioration of FRP bars but does not offer any model to predict bond strength degradation of FRP adhesive anchors under WD cycles. Existing models on FRP–concrete bonds under WD exposure [17–22] were developed for EB or NSM FRP systems or for two-phase systems (FRP bar directly bonded to concrete without an adhesive layer). None of these models account for the presence of an epoxy adhesive layer or the bonded length effect. To the best of our knowledge, the proposed model is the first to predict the interfacial bond strength degradation of FRP adhesive anchors in concrete induced by WD cycles. The degradation trends observed in this study are also consistent with the bond mechanisms reported by Zeng et al. [26] for GFRP bars embedded in ultra-high-strength concrete, where bond strength was governed by either the shear resistance of the concrete or the resin–fiber interface, depending on the relative strengths. Under WD cycles, the weakening of the epoxy adhesive shifts the controlling interface from bar–adhesive to adhesive–concrete, a mechanism that has not been previously reported for ETS FRP systems.

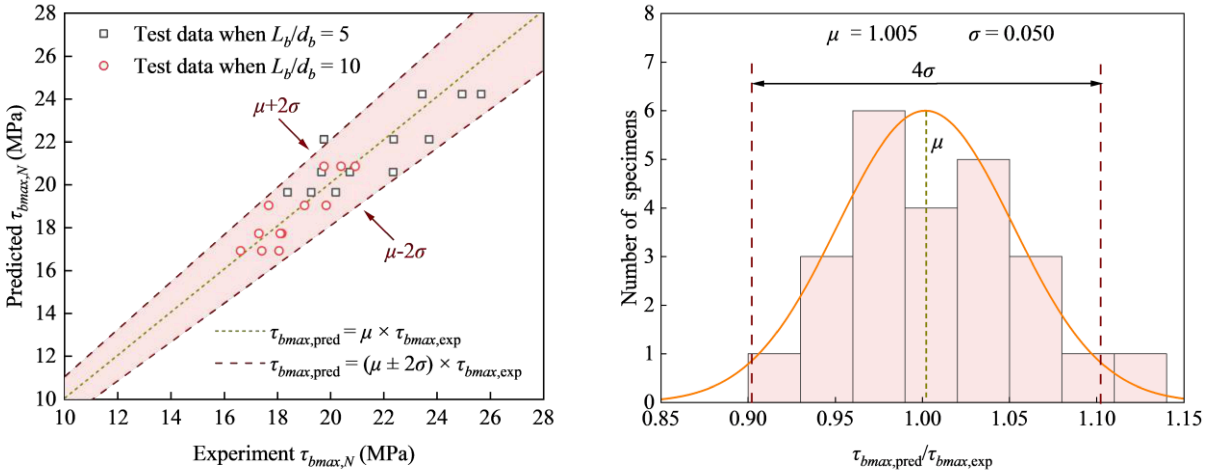

Figure 13. Evaluation of predicted bond strength against experimental data: (**a**) correlation of predicted and measured values; (**b**) distribution pattern of prediction to experiment ratios. Note that this figure shows the goodness of fit on the calibration data. Independent validation was not possible due to the lack of existing data on FRP adhesive anchors under WD cycles.

To further validate the difference between the present test results and those reported in existing studies, a detailed quantitative comparison is made with the NSM FRP system studied by Gong et al. [27]. In their study, NSM CFRP bars were embedded in concrete with epoxy adhesive under almost the same WD cycles of 0, 30, 70, and 90. The bond strength of the NSM CFRP bars decreased by approximately 24.74% after 30 cycles, 23.85% after 70 cycles, and 25.08% after 90 cycles, with most degradation occurring within the first 30 cycles. In our experiments on the ETS GFRP system, the bond strength losses after 30 cycles were 11.10% for the specimens with a bonded length of 40 mm (five times the bar diameter) and 8.16% for those with a bonded length of 80 mm (10 times the bar diameter). After 90 cycles, the losses were 21.87% for the 40 mm bonded length and 14.72% for the 80 mm bonded length. The lower degradation in the ETS FRP system, particularly for the longer bonded length, is attributed to the larger concrete cover that better protects the bonded interface from moisture and ion ingress. Nevertheless, both systems exhibit a similar nonlinear degradation pattern featuring rapid initial loss followed by gradual stabilization, which indicates a common underlying interfacial damage mechanism. This comparison does not constitute independent validation of the proposed model but provides contextual evidence that the observed degradation trend is consistent with a different FRP system and supports the applicability of our model for the ETS FRP system.

To verify the accuracy of the bond strength degradation model, Figure 13 shows a comparison between the bond strength values predicted by Equation (13) and the experimental results for all test groups. The model demonstrates good predictive capability, with the majority of data points falling within the ±10% error bands. Further statistical analysis reveals that the mean predicted-to-experimental ratio (μ) is 1.005, with a coefficient of variation (COV) of 5.0%. The 95% confidence interval for the relative error is around ±11.3%, indicating acceptable accuracy for engineering applications.

The presented model effectively reproduces two key experimental trends: (i) a nonlinear degradation pattern characterized by rapid initial decline followed by gradual stabilization; and (ii) a clear bonded length effect, where longer bond lengths exhibit slower degradation than shorter ones. This is quantitatively reflected in the coefficients of Equation (10), i.e., the linear term coefficient for $L_b/d_b = 10$ is approximately 30% smaller in magnitude than that for $L_b/d_b = 5$ (−0.00616), confirming the reduced degradation rate. This can be explained by the "reserve length" effect that has been discussed in Section 3.4.

4.3. Practical Applications and Limitations

The practical implications of the proposed bond strength degradation model are twofold. First, they enable engineers to estimate the remaining bond strength of GFRP adhesive anchors after a given number of WD cycles, facilitating service life assessment and maintenance planning for coastal infrastructure. Second, the explicit incorporation of bonded length effects allows for the optimization of anchorage design to achieve desired durability performance, for instance, selecting longer bond lengths in zones of severe environmental exposure to leverage the enhanced durability conferred by the "reserve length" mechanism.

From a financial standpoint, the design of GFRP-bonded anchor systems intended for marine environments with WD cycling requires optimization between upfront material expenses and extended service performance. The findings reported here indicate that conventional epoxy adhesives, despite their cost-effectiveness, undergo gradual deterioration in the bond capacity when subjected to cyclic exposure conditions. This degradation, if unaccounted for, may lead to reduced service life and increased maintenance costs over the structure's lifetime. Conversely, epoxy formulations with enhanced moisture resistance, such as those incorporating hydrophobic additives or modified resin chemistries, can provide better bond retention under WD cycles but typically incur higher costs, often 1.5 to 2 times that of standard products [20,46,47]. The selection of an appropriate adhesive therefore requires a lifecycle cost analysis that weighs initial investment against anticipated maintenance intervals and replacement costs.

With regard to durability design, a cost-effective strategy is the optimization of anchor geometry rather than reliance solely on material property upgrades [48,49]. Longer bonded lengths exhibit superior durability under WD cycles owing to the "reserve length" effect, where the bonded portion away from the loaded end remains relatively protected from environmental attack. This finding offers designers a practical means of enhancing durability without incurring the premium costs associated with specialized adhesive formulations. For critical anchorage zones subject to severe exposure, such as tidal and splash zones in marine structures, specifying increased bonded length may prove more economical than specifying high-cost, moisture-resistant adhesives, particularly in cases of large infrastructure projects. Overall, this work presents the first step towards the bond behavior and degradation mechanism of adhesively bonded GFRP bars in concrete under WD cycles. However, there are several limitations required to be addressed in future studies.

First, the proposed model is purely empirical and was calibrated for a specific set of experimental conditions. These conditions include C50 concrete with a compressive strength of 53.96 MPa, sand-coated GFRP bars of 8 mm diameter, a constant concrete cover-to-bar diameter ratio c/d_b of 5.75, and WD cycles up to 90. The model does not explicitly account for variations in concrete strength, cover thickness, adhesive type, FRP bar type, bar diameter, and bar surface treatments. Its applicability to other conditions is therefore limited. The proposed model has not been validated against independent external experimental data. The model was calibrated solely using the results of this work. While cross-validation demonstrated internal consistency, external validation using datasets from different laboratories, material batches, or environmental conditions is necessary before the model can be confidently applied beyond the specific conditions investigated herein. This limitation is particularly important given the empirical nature of the model and the absence of comparable studies on GFRP adhesive anchors under WD cycles in the existing literature. Future work should extend the model by testing a wider range of these variables. Until then, the model should be applied only within the parameter ranges investigated in this study.

Second, all degradation mechanisms discussed herein are inferred from macroscopic measurements such as bond strength loss, stiffness degradation, and failure mode observations. However, the interpretation of degradation mechanisms is still not supported by microstructural analysis [e.g., scanning electron microscopy (SEM), mercury intrusion porosimetry (MIP), or X-ray diffraction (XRD)] to verify the damage processes at the adhesive, the interfacial transition zone (ITZ) of concrete, or the GFRP bar surface. This absence of microstructural analysis limits the depth of mechanistic interpretation and represents a clear limitation of the present work. As demonstrated by Hu et al. [50], techniques such as acoustic emission and computed tomography can effectively capture damage evolution in concrete under coupled environmental actions, while Liu et al. [51] showed that fiber–matrix interface bonding critically affects the macroscopic toughness of cementitious composites. Future advanced microstructural characterization should be employed to directly link macroscopic observations to micro-scale damage evolution.

Third, a reliable bond stress–slip constitutive relationship is fundamental for evaluating the anchorage performance of GFRP adhesive anchors, enabling accurate simulation of their pull-out response under WD cycling conditions. Therefore, it is desirable to incorporate cycle-dependent bond stress–slip constitutive laws for the GFRP anchor-to-concrete interface into numerical models or theoretical analyses. The development of such a bond–slip degradation constitutive model is currently underway.

Fourth, the experimental program employed three replicates per test group. Although this sample size is typical in many bond durability studies and the ANOVA results showed statistically significant differences between cycle levels, the limited number of specimens increases the uncertainty in estimating variability, especially for post-peak parameters. Future studies with larger sample sizes (e.g., $n \geq 6$) would provide more robust statistical characterization of bond degradation under WD cycles.

It is worth noting that the maximum of 90 WD cycles is far from sufficient to represent long-term marine exposure. Although this range is consistent with typical accelerated laboratory protocols for FRP–concrete bond durability [20,27,36], longer-term exposure (e.g., up to 110 months as reported by Hao et al. [37]) would likely cause additional bond degradation. Their study demonstrated that bond degradation continued over longer periods while the degradation rate decreased with time. Therefore, the proposed model should not be extrapolated beyond 90 cycles without further experimental validation. Further experimental investigations with extended cycling up to 360 cycles or more should be conducted to develop a more comprehensive long-term predictive model for bond durability.

5. Conclusions

This paper has presented an experimental study on the effect of WD cycles on the bond performance between GFRP adhesive anchors and concrete. Based on the test results, the following conclusions are drawn.

(1) The failure mode shifts progressively from the bar–adhesive interface to the adhesive–concrete interface as the number of WD cycles increases. This transition is caused by cumulative degradation of the adhesive, softening of the ITZ of concrete, and deterioration of the GFRP bar surface layer. After 90 cycles, adhesive splitting, which was prominent in unexposed specimens, is no longer observed.

(2) Bond strength and residual bond strength decrease markedly with increasing WD cycles, with the most pronounced degradation occurring within the first 30 cycles. Residual bond strength is more sensitive to cyclic exposure than peak bond strength, indicating that post-peak frictional resistance is strongly affected by WD exposure.

(3) Longer bonded lengths provide superior durability under WD cycles. The enhanced durability of longer bars is explained by the reserve length effect, in which the bonded

area away from the loaded end remains partially protected from environmental attack and continues to contribute to load transfer as degradation progresses. This finding has practical implications for the design of FRP bars in aggressive environments.

(4) The proposed bond strength degradation model is the first to explicitly account for both the number of WD cycles and the bonded length of adhesively bonded FRP bars. The model requires only the undegraded compressive strength of concrete as input and is validated with good accuracy. It fills a critical gap in current design guidelines (e.g., ACI 440.3R-15), which do not provide provisions for bond degradation in FRP bars under WD exposure.

(5) The adhesively bonded FRP bars exhibit superior durability compared to the NSM FRP system under identical WD cycles. This advantage arises from the larger concrete cover, which delays moisture and ion ingress to the bonded interface. The finding demonstrates the potential of adhesively bonded FRP bars to serve as a durable alternative to the NSM FRP system for long-term performance in marine environments.

(6) More generally, this study highlights the need to incorporate cycle-dependent degradation models into durability design frameworks for FRP-strengthened concrete structures in coastal and marine environments. The proposed model provides a practical tool for such purposes, though further research is needed to extend its applicability to different concrete strengths, cover thicknesses, adhesive formulations, bar diameters, FRP types, and surface treatments.

It should be noted that the proposed model was calibrated on the experimental data of this study and its internal robustness was verified through cross-validation. Independent validation was not possible due to the absence of comparable data on FRP adhesive anchors under WD cycles in the literature. Therefore, the model should be applied only within the parameter ranges investigated herein, and further experimental validation is currently underway.

Author Contributions: Conceptualization, Y.W. and W.L.; methodology, Y.W.; software, X.D.; validation, X.D. and Y.X.; formal analysis, Y.X.; investigation, Y.X.; resources, Y.W.; data curation, W.L.; writing—original draft preparation, Y.X.; writing—review and editing, Y.W.; visualization, Y.X. and Y.W.; supervision, Y.W.; project administration, Y.W.; funding acquisition, Y.W. All authors have read and agreed to the published version of the manuscript.

Funding: This research was founded by the National Natural Science Foundation of China (Grant No. 52308165) and China Postdoctoral Science Foundation (Grant No. 2023M732607). Yan-Jie Wang thanks the China Scholarship Council (No. 202208130081) for their financial support and for his visit to the University of Western Australia.

Data Availability Statement: The original contributions presented in this study are included in the article material.

Conflicts of Interest: The authors declare no conflicts of interest.

References

1. González, F.; Fernández, J.; Agranati, G.; Villanueva, P. Influence of construction conditions on strength of post installed bonded anchors. *Constr. Build. Mater.* **2018**, *165*, 272–283. [CrossRef]
2. Alhaidary, H.; Al-Tamimi, A.K. Importance of performance certification for post-installed anchors: An experimental assessment. *Structures* **2021**, *29*, 273–285. [CrossRef]
3. Li, A.; Cheng, H.; Yue, Z.; Rong, C. Mechanical performance analysis of fully grouted bolts in tunnels considering the effect of confining pressure. *Tunn. Undergr. Space Technol.* **2026**, *168*, 107222. [CrossRef]
4. Stehle, E.J.; Sharma, A. Review of testing and qualification of post-installed anchors under seismic actions for structural applications. *CivilEng* **2021**, *2*, 406–420. [CrossRef]

5. Neupane, C.C.; Lee, J.; Pokharel, T.; Tsang, H.H.; Gad, E. Development and challenges in finite element modelling of post-installed anchors in concrete. *Struct. Infrastruct. Eng.* **2025**, *21*, 319–340. [CrossRef]
6. Sun, G.; Yan, N.; Bai, X.; Liu, J.; Hou, D.; Sang, S.; Zhang, M.; Wang, P.; Jing, D. Laboratory full-scale test on the bond property of GFRP anchor to concrete. *Constr. Build. Mater.* **2023**, *396*, 132216. [CrossRef]
7. Ren, Y.; Wang, H.; Guan, Z.; Yang, K. Evaluation of the properties and applications of FRP bars and anchors: A review. *Rev. Adv. Mater. Sci.* **2023**, *62*, 20220287. [CrossRef]
8. Kazemi, H.; Yekrangnia, M.; Shakiba, M.; Bazli, M.; Vatani Oskouei, A. Bond durability between anchored GFRP bar and seawater concrete under offshore environmental conditions. *Mater. Struct.* **2023**, *56*, 64. [CrossRef]
9. Ahmed, E.A.; El-Salakawy, E.F.; Benmokrane, B. Tensile capacity of GFRP postinstalled adhesive anchors in concrete. *J. Compos. Constr.* **2008**, *12*, 596–607. [CrossRef]
10. Liang, W.; Lu, J.; Fu, J.; Zhang, B.; Wang, Y. Analytical and Experimental Study on Bond Behavior of Embedded Through-Section FRP Bar-to-Concrete Joints Using a Trilinear Cohesive Material Law. *Buildings* **2025**, *16*, 164. [CrossRef]
11. Zuo, D.; Wang, Y.; Qi, S.; Wu, Z. Temperature-dependent bond behavior between GFRP adhesive anchors and concrete: An experimental study. *Structures* **2026**, *85*, 111120. [CrossRef]
12. Liu, H.; Ma, D.; Wang, Y.; Guo, Z.; Jia, M.; Wu, Z.; Gao, Y. Experimental and analytical study of bond-slip behavior of ETS GFRP bar-to-concrete joints subjected to elevated temperatures. *Eng. Struct.* **2025**, *343*, 121085. [CrossRef]
13. Wang, Y.J.; Liu, H.B.; Ma, D.; Zhang, G.Q.; Wu, Z.M.; Jia, M.D. Experimental and analytical investigations on debonding response of embedded through-section ribbed GFRP bar-to-concrete joints at elevated temperatures. *Constr. Build. Mater.* **2024**, *447*, 138000. [CrossRef]
14. Godat, A.; L'Hady, A.; Chaallal, O.; Neale, L.W. Bond behavior of the ETS FRP bar shear-strengthening method. *J. Compos. Constr.* **2012**, *16*, 529–539. [CrossRef]
15. Caro, M.; Jemaa, Y.; Dirar, S.; Quinn, A. Bond performance of deep embedment FRP bars epoxy-bonded into concrete. *Eng. Struct.* **2017**, *147*, 448–457. [CrossRef]
16. Zhao, J.; Mei, K.; Wu, J. Long-term mechanical properties of FRP tendon–anchor systems—A review. *Constr. Build. Mater.* **2020**, *230*, 117017. [CrossRef]
17. Garzón-Roca, J.; Sena-Cruz, J.M.; Fernandes, P.; Xavier, J. Effect of wet-dry cycles on the bond behaviour of concrete elements strengthened with NSM CFRP laminate strips. *Compos. Struct.* **2015**, *132*, 331–340. [CrossRef]
18. Wang, Y.L.; Guo, X.Y.; Shu, S.Y.H.; Guo, Y.C.; Qin, X.M. Effect of salt solution wet-dry cycling on the bond behavior of FRP-concrete interface. *Constr. Build. Mater.* **2020**, *254*, 119317. [CrossRef]
19. Noor-E.-Khuda, S. Influence of wetting-drying cycles on compressive and flexural strength of cement mortar and CFRP-mortar bond strength. *Constr. Build. Mater.* **2021**, *271*, 121513. [CrossRef]
20. Cui, E.; Jiang, S.; Wang, J.; Zeng, X. Bond behavior of CFRP-concrete bonding interface considering degradation of epoxy primer under wet-dry cycles. *Constr. Build. Mater.* **2021**, *292*, 123286. [CrossRef]
21. Wei, M.W.; Xie, J.H.; Zhang, H.; Li, J.L. Bond-slip behaviors of BFRP-to-concrete interfaces exposed to wet/dry cycles in chloride environment. *Compos. Struct.* **2019**, *219*, 185–193. [CrossRef]
22. Al-Lami, K.; Colombi, P.; D'Antino, T. Experimental and numerical analysis of CFRP-concrete joint bond behavior after exposure to wet-dry cycles. *Compos. Struct.* **2023**, *303*, 116273. [CrossRef]
23. Xie, J.; Li, J.; Lu, Z.; Zhang, H. Experimental Study on Fatigue Behaviour of BFRP-Concrete Bond Interfaces under Bending Load. *Shock Vib.* **2018**, *2018*, 7497061. [CrossRef]
24. Xie, J.H.; Wei, M.W.; Huang, P.Y.; Zhang, H.; Chen, P.S. Fatigue behavior of the basalt fiber-reinforced polymer/concrete interface under wet-dry cycling in a marine environment. *Constr. Build. Mater.* **2019**, *228*, 117065. [CrossRef]
25. Cunha, A., Jr.; Yanik, Y.; Olivieri, C.; Da Silva, S. Tresca versus Von Mises: Which failure criterion is more conservative in a probabilistic context? *J. Appl. Mech.* **2024**, *91*, 111008. [CrossRef]
26. Zeng, J.J.; Liao, J.J.; Zhuge, Y.; Guo, Y.C.; Zhou, J.K.; Huang, Z.H.; Zhang, L. Bond behavior between GFRP bars and seawater sea-sand fiber-reinforced ultra-high strength concrete. *Eng. Struct.* **2022**, *254*, 113787. [CrossRef]
27. Gong, J.Z.; Yang, S.T.; Liu, Y. Experimental study on bond performance of NSM CFRP bars with concrete under chloride solution wet-dry cycling environment. *Fiber Reinf. Plast. Compos.* **2018**, *4*, 11–14. (In Chinese)
28. *ASTM D3916-08*; Standard Test Method for Tensile Properties of Pultruded Glass-Fiber-Reinforced Plastic Rod. ASTM International: West Conshohocken, PA, USA, 2016.
29. *JGJ 55-2011*; Specification for Mix Proportion Design of Ordinary Concrete. China Architecture and Building Press: Beijing, China, 2011. (In Chinese)
30. *GB/T 50081-2019*; Standard for Test Methods of Concrete Physical and Mechanical Properties. China Building and Construction Press: Beijing, China, 2019. (In Chinese)
31. *GB/T 2567-2008*; Test Methods for Properties of Resin Casting Body. Standards Press of China: Beijing, China, 2008. (In Chinese)

32. *ASTM D1141-98*; ASTM standard for Standard Practice for the Preparation of Substitute Ocean Water, Designation: D 1141-98 (Reapproved 2003). ASTM International: West Conshohocken, PA, USA, 2003.
33. Singh, A.; Dayu, X.; Ituen, E.; Ansari, K.; Quraishi, M.A.; Kaya, S.; Lin, Y. Tobacco extracted from the discarded cigarettes as an inhibitor of copper and zinc corrosion in an ASTM standard D1141-98 (2013) artificial seawater solution. *J. Mater. Res. Technol.* **2020**, *9*, 5161–5173. [CrossRef]
34. *GB/T 30022-2013*; Test Method for Basic Mechanical Properties of Fiber Reinforced Polymer Bar. China Architecture & Building Press: Beijing, China, 2015. (In Chinese)
35. *GB/T 50082-2024*; Standard for Test Methods of Long-Term Performance and Durability of Ordinary Concrete. China Architecture & Building Press: Beijing, China, 2009. (In Chinese)
36. Song, H.; Jiang, S.; Zang, R.; Jin, L.; Cui, E. Bond behavior of CFRP-concrete with surface groove subjected to chloride wet-dry cycles: Experimental, strength model and design method. *Thin-Walled Struct.* **2024**, *195*, 111499. [CrossRef]
37. Hao, Z.H.; Zeng, J.J.; Chen, G.M.; Dai, J.G.; Chen, J.F. Durability of FRP-to-concrete bonded joints subjected to 110 months accelerated laboratory and field exposure. *Eng. Struct.* **2024**, *305*, 117681. [CrossRef]
38. Rosa, I.C.; Firmo, J.P.; Correia, J.R.; Barris, J.A.O. Bond behaviour of sand coated GFRP bars to concrete at elevated temperature-Definition of bond vs. slip relations. *Compos. Part B Eng.* **2019**, *160*, 329–340. [CrossRef]
39. Yang, Z.; Lu, C.; Yuan, S.; Ge, H. Effect of mechanical interlocking damage on bond durability of ribbed and sand-coated GFRP bars embedded in concrete under chloride dry-wet exposure. *Polymers* **2025**, *17*, 733. [CrossRef]
40. Yan, F.; Lin, Z.; Yang, M. Bond mechanism and bond strength of GFRP bars to concrete: A review. *Compos. Part B Eng.* **2016**, *98*, 56–69. [CrossRef]
41. Ha, K.; Choi, H.; Shin, M.; Park, K. On the size effect of interfacial fracture between concrete and fiber reinforced polymer. *Cem. Concr. Compos.* **2018**, *93*, 99–106. [CrossRef]
42. *ACI 440.3R-15*; Guide Test Methods for Fiber-Reinforced Polymers (FRPs) for Reinforcing or Strengthening Concrete Structures. American Concrete Institute: Farmington Hills, MI, USA, 2015.
43. Yang, Z.; Yuan, S.; Lu, C.; Ge, H. Experiment and calculation investigations on bond durability of ribbed and sand-coated GFRP bars embedded in concrete under chloride dry-wet exposure. *Adv. Struct. Eng.* **2025**, 13694332251381222. [CrossRef]
44. Ke, L.; Li, L.; Feng, Z.; Chen, G.; Li, Y. Temperature-dependent bond-slip behavior of CFRP bars embedded in ultrahigh-performance fiber-reinforced concrete. *J. Compos. Constr. ASCE* **2024**, *28*, 04023070. [CrossRef]
45. Sturm, R.; Fam, A. Bond and development length of GFRP bars embedded in shotcrete. *J. Compos. Constr.* **2025**, *29*, 04025025. [CrossRef]
46. Montazeri, S.H.; Ranjbar, Z.; Rastegar, S.; Deflorian, F. A new approach to estimates the adhesion durability of an epoxy coating through wet and dry cycles using creep-recovery modeling. *Prog. Org. Coat.* **2021**, *159*, 106442. [CrossRef]
47. Xie, J.; Lu, Z.; Guo, Y.; Deflorian, F. Durability of CFRP sheets and epoxy resin exposed to natural hygrothermal or cyclic wet-dry environment. *Polym. Compos.* **2019**, *40*, 553–567. [CrossRef]
48. Sun, W.; Zhao, J.; Li, Q.; Xiao, Z. Experimentally optimized anchored-FRP method: A high-strength, cost-effective and ease-to-install technique for concrete rehabilitation. *Case Stud. Constr. Mater.* **2024**, *21*, e03927. [CrossRef]
49. Hao, Z.; Liu, H.; Yan, N.; Wang, Z.; Bai, X.; Han, J.; Mi, C.; Jia, S.; Sun, G.; Zhu, L.; et al. In-situ test and numerical simulation of anchoring performance of embedded rock GFRP anchor. *Buildings* **2023**, *13*, 2799. [CrossRef]
50. Hu, Z.; Yang, Y.W.; Zhang, H. Durability and damage evolution of steel fiber and Nano-SiO_2 reinforced concrete under freeze-thaw and salt erosion environments based on acoustic emission and Computed Tomography analysis. *J. Build. Eng.* **2025**, *115*, 114595. [CrossRef]
51. Liu, Z.; Qi, X.; Ke, J.; Shui, Z. Enhancing the toughness of ultra-high performance concrete through improved fiber-matrix interface bonding. *Constr. Build. Mater.* **2025**, *491*, 142616. [CrossRef]

Disclaimer/Publisher's Note: The statements, opinions and data contained in all publications are solely those of the individual author(s) and contributor(s) and not of MDPI and/or the editor(s). MDPI and/or the editor(s) disclaim responsibility for any injury to people or property resulting from any ideas, methods, instructions or products referred to in the content.